Sensors and Actuators Reports 4 (2022) 100081

Contents lists available at ScienceDirect

Sensors and Actuators Reports

journal homepage: www.sciencedirect.com/journal/sensors-and-actuators-reports

Light-assisted ozone gas-sensing performance of SnO_2 nanoparticles: Experimental and theoretical insights

João V.N. de Palma [a], Ariadne C. Catto [b], Marisa C. de Oliveira [b], Renan A.P. Ribeiro [c], Marcio D. Teodoro [d], Luís F. da Silva [a,*]

[a] Laboratory of Nanostructured Multifunctional Materials, Federal University of São Carlos, São Carlos, SP, Brazil
[b] Center for the Development of Functional Materials, Federal University of São Carlos, São Carlos, SP, Brazil
[c] Laboratory of Theoretical Chemistry and Computational Modelling, Minas Gerais State University, Divinópolis, MG, Brazil
[d] Department of Physics, Federal University of São Carlos, 13565-090, São Carlos, SP, Brazil

ARTICLE INFO

Keywords:
SnO_2
Nanoparticles
Chemiresistor
Light-assisted
Ozone
DFT calculations

ABSTRACT

We report herein an investigation on the ozone gas-sensing performance at room temperature of SnO_2 nanoparticles assisted by a light-emitting diode. X-ray diffraction and high-resolution transmission electron microscopy analyses indicated the nanocrystalline characteristics of the SnO_2 particles after heat treatment. Besides, optical measurements pointed out that the nanoparticles presented an optical gap of approximately 3.8 eV with a broad photoluminescence emission at around 625 nm, which was linked to the presence of oxygen vacancies, suggested by XPS analysis. With regard to the light-assisted gas-sensing measurements, electrical analysis revealed a clear dependence of the ozone sensing performance on the wavelength of the source of illumination chosen, with the highest ozone response being reached upon excitation in the ultraviolet region. Theoretical calculations showed that the (110) surface could increase the stability of photogenerated carriers and contribute to enhancing the gas-sensing features under ultraviolet excitation due to the presence of $[SnO_6]$ and $[SnO_5]$ clusters, which are capable of inducing an electron-hole dissociation and a reliable chemical environment for O_3 interaction.

1. Introduction

Metal semiconducting oxides (MOXs) have attracted growing attention due to their potential in diverse practical applications, including resistive gas sensors. [1–5] With regard to resistive gas sensors or chemiresistors, they have been investigated for the detection of various analytes, mainly harmful species, such as NO_x, CO, NH_3, H_2S, and O_3. [1,6–9] According to the literature, chemiresistors based on MOXs have worked at relatively high temperatures, i.e., superior to 150 °C. To achieve such temperatures, self-heaters have been made up in the structure of the device, thus involving more complexity in the manufacturing steps, besides increasing the energy consumption of the such devices. [10–12] Note that these operating temperatures may provoke permanent changes in the chemical and structural characteristics of the sensing layer, impairing its lifetime. [13,14]

In this sense, researchers have focused on the development of sensing materials with high sensitivity and selectivity, and fair stability, apart from operating at moderate temperatures (preferably close to room temperature). An efficient and versatile strategy to achieve sensitivity has been the full or partial replacement of the conventional thermal activation by light stimulation. [10,11,15–17] The irradiation of the sensing materials with a low-energy consumption source such as light-emitting diodes (LEDs) has provided promising results. In previous works, we reported that the ozone gas-sensing properties of ZnO-SnO_2 nanocomposites and pristine ZnO were improved when the materials were kept under continuous UV illumination. [15,18] In another study, Gonzalez et al. combined thermal and light stimulations to enhance the sensing performance of WO_3 nanoneedles. [11,19] They reported that the combination of mild heating ($\leq$ 100°C) with pulsed UV light irradiation of the sensing layer resulted in a significant increase in the sensing activity of the WO_3. [19]

Among the various MOXs investigated as light-assisted sensing materials, tin dioxide (SnO_2) has been applied for the detection of a wide range of analytes. [20–22] In its stoichiometric form, this compound acts as an insulator, while the $SnO_{2-\delta}$ behaves as an n-type semiconductor with a band gap of approximately 3.6 eV at 300 K. [23] The

* Corresponding author:
E-mail address: lfsilva83@gmail.com (L.F. da Silva).

https://doi.org/10.1016/j.snr.2022.100081
Received 12 December 2021; Received in revised form 14 January 2022; Accepted 27 January 2022
Available online 7 February 2022
2666-0539/© 2022 The Author(s). Published by Elsevier B.V. This is an open access article under the CC BY-NC-ND license (http://creativecommons.org/licenses/by-nc-nd/4.0/).

presence of such defects in the SnO_2 network, e.g. oxygen vacancies, has allowed the use of wavelength in the visible region to stimulate its gas-sensing properties at room temperature. [24–29] For example, Anothainart et al. reported the NO_2 sensing properties of the SnO_2 compound under visible illumination at room temperature. [24] They observed that the photoexcitation with wavelengths smaller than 600 nm was enough to activate the adsorption mechanism of SnO_2. Despite the fact that ozone gas sensors based on SnO_2 compound are widely studied, few papers have specifically studied of the effect of wavelength on the light-assisted ozone sensing performance of SnO_2. Motivated by these considerations, we investigate herein the role played by the different wavelengths employed to assist the ozone gas sensing experiments using SnO_2 nanoparticles as a sensing layer. For this purpose, experimental and theoretical approaches were employed in order to evaluate the SnO_2 sensing activity. X-ray diffraction, transmission electron microscopy, optical spectroscopies, and electrical measurements were performed along with first-principles calculations to get insight into the electronic properties of adsorption of O_3 molecules on the SnO_2 surfaces.

2. Experimental section

2.1. 2.1. Synthesis of SnO_2 nanoparticles

The SnO_2 nanoparticles were synthesized via hydrolysis of tin chloride, followed by thermal treatment. The tin (II) chloride ($SnCl_2.6H_2O$, 99.9%) and ethyl alcohol anhydrous (CH_3CH_2OH, 99.5%) were purchased from Sigma-Aldrich Corporation and used without any further purification. The tin chloride (0.1 M) was dissolved in 100 mL of ethyl alcohol under constant stirring at room temperature. Then, 22.5 mL of deionized water was dropped into the solution, which was kept under stirring for 30 min. To remove the chlorides from the solution, the dialysis process was performed, and the obtained precipitate was dried in an electric oven at 80 °C overnight. The as-obtained powder had an amorphous characteristic, revealed by X-ray diffraction analysis. To obtain a crystalline sample, it was annealed in an electric oven for 1 h at 500°C under an air atmosphere.

2.2. 2.2. Characterization techniques

X-ray diffraction measurements were collected using a Shimadzu diffractometer (XRD6100, CuKα radiation) in the 2θ range from 20^o to 80^o with a step of 0.02, and at scanning speed of 2^o min^{-1}. Ultraviolet-visible diffuse reflectance spectrum (UV-vis DRS) was collected on a spectrophotometer (Shimadzu, UV-2600) coupled to an integrating sphere from 200 to 800 nm. The morphological features were investigated using a high-resolution transmission electron microscopy (HRTEM, FEI Tecnai G2 F20) operating at 200 KeV. Room temperature photoluminescence (PL) measurements were performed using a 355 nm laser as the excitation source, focused on a 200 μm spot at constant power of 5 mW. The luminescence signal was dispersed by a 19.3 cm spectrometer (Andor/Kymera) and detected by a Si charge-coupled device (Andor/Idus BU2).

2.3. 2.3. Gas-sensing experiments

To perform the ozone gas-sensing measurements, the sensors were prepared following a procedure commonly adopted by our team [15, 30–32]. First, 50 mg of the sample was dispersed in 0.5 mL of isopropyl alcohol using an ultrasonic cleaner. The obtained suspension was then dripped onto a SiO_2/Si substrate with 120 nm thick Pt electrodes separated by a distance of 50 mm. To remove the solvents in the suspension, the sensor sample was annealed for 30 min at 500°C in an electric oven. Afterwards, the sensor sample was inserted into a special chamber that allows the control of the substrate temperature, the gas flow, and the O_3 levels. The O_3 gas was generated using a calibrated pen-ray UV lamp, providing concentrations ranging from 12 to 94 ppb. In these dynamic experiments, the dry air (carrier gas) containing O_3 gas was blown directly onto the sample, keeping a constant flux of 500 SCCM. Further details regarding the gas-sensing workbench may be found in our previous works. [30,31,33,34] The electrical resistance of the sample was monitored with an electrometer (Keithley, 6514) by applying a voltage of 1 V (*DC*). All measurements were carried out at room temperature (25 ± 1 °C) under continuous light irradiation provided by a light-emitting diode (LED) 10 mm distant from the sensing sample. The wavelengths studied here were UV (315 nm, 0.6 mW), violet (405 nm, 10 mW), and blue (465 nm, 20 mW). Longer wavelengths were also investigated, however, no influence on the sensing performance was found. It is worth mentioning that for each experiment using a certain LED, the studied sample was kept in a dark chamber overnight to protect it from any previous light stimulation. The sensor response (S) was defined as $S=R_{O3}/R_{air}$, where R_{O3} and R_{air} are the electric resistance of the sensor exposed to O_3 gas and dry air, respectively. [15,31,32]

2.4. 2.4. Computational methods

Theoretical calculations based on the Density Functional Theory were carried out by combining hybrid B3LYP [35,36] functional and two- and three-body contributions to the long-range dispersion energy (B3LYP-D3), [37] as implemented in the CRYSTAL17 code. [38] Herein, bulk and surface models were used to investigate the O_3 gas sensing properties of SnO_2. The tetragonal rutile phase was generated from XRD data, while the non-polar (100) and (110) surfaces were constructed using symmetrical and stoichiometric slabs. Durand–Barthelat (DB) core pseudopotentials were used for Sn atoms [Kr]5s25p2, whereas O centers were described with all-electron 6-31G* basis set, following previous theoretical studies for bulk and surface SnO_2 models. [39–41] The electronic integration over the Brillouin Zone was performed using a 8 × 8 × 8Monkhorst–Pack k-mesh. [42] Five thresholds were set to 8, 8, 8, 8, and 16 in order to control the accuracy of the Coulomb and exchange integral calculations. The convergence criteria for mono and bielectronic integrals were set to 10^{-8} Hartree, while the RMS gradient, RMS displacement, maximum gradient, and maximum displacement were set to 3×10^{-4}, 1.2×10^{-3}, 4.5×10^{-4} and 1.8×10^{-3} a.u., respectively. The electronic properties were evaluated through the density of states (DOS), band structure profiles, and charge analysis tools implemented in the CRYSTAL17 code. [38]

Aiming to investigate the O_3 sensing properties of the SnO_2 samples, adsorption models were constructed from (2 × 2) supercell expansions of previously optimized slabs. The adsorption enthalpy was calculated considering the expressions:

$$E_{ads} = \frac{1}{N}\left[E_{(slab+O_3)} - \left(E_{slab} + NE_{O_3}\right) + E_{BSSE}\right] \quad (1)$$

$$E_{BSSE} = \left(E_{slab}^{frozen} - E_{slab+ghpst}^{frozen}\right) + \left(E_{O_3}^{frozen} - E_{O_3+ghpst}^{frozen}\right) \quad (2)$$

here $E_{(slab+O_3)}$ is the total energy of the optimized slab with adsorbed O_3 molecule, $\boldsymbol{E_{slab}}$ is the total energy of the isolated optimized slab, N is the number of adsorbed O_3 molecules per unit cell and $\boldsymbol{E_{O3}}$ is the total energy of ozone in the gas phase. The basis set superposition error (BSSE) was calculated considering the two separated moieties (slab + O_3) frozen in the minimum adsorption configuration, with and without ghost functions, respectively.

The photo-assisted O_3 sensing properties were evaluated considering the existence of excited electrons and holes through the localization of charge doping levels using the keyword DOPING, which allows adding (or removing) electrons to (from) the system. [38]

3. Results and Discussions

X-ray diffraction (XRD) patterns of the SnO_2 samples before and after

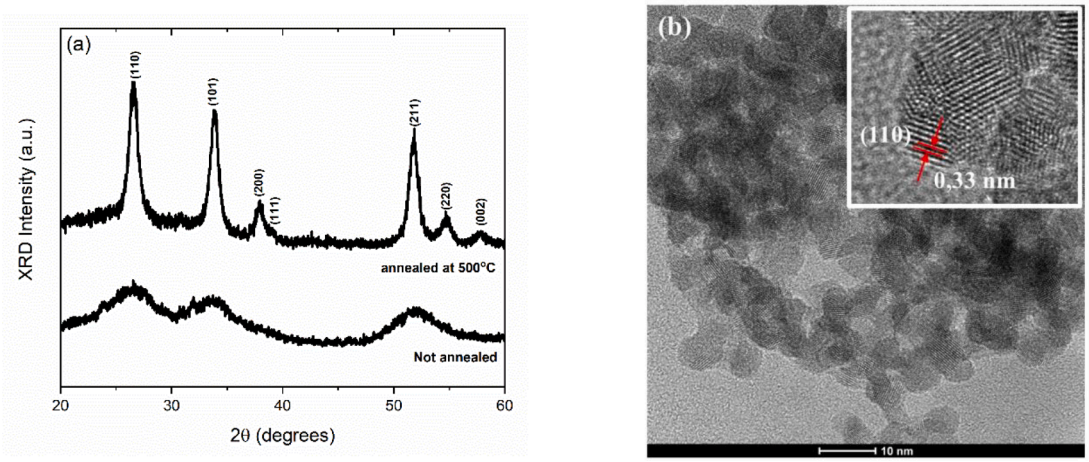

Fig. 1. (a) XRD patterns of SnO_2 samples before and after heat treatment. (b) HRTEM micrograph of the annealed sample. The inset in Fig.(b) shows the interplanar distance of the nanocrystalline SnO_2 sample.

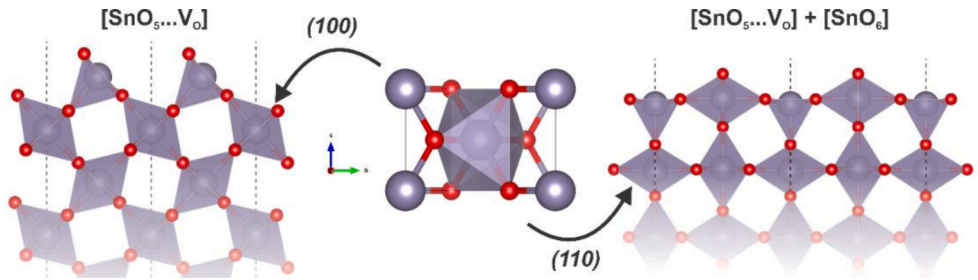

Fig. 2. Optimized crystalline structures for SnO_2 bulk and surface models.

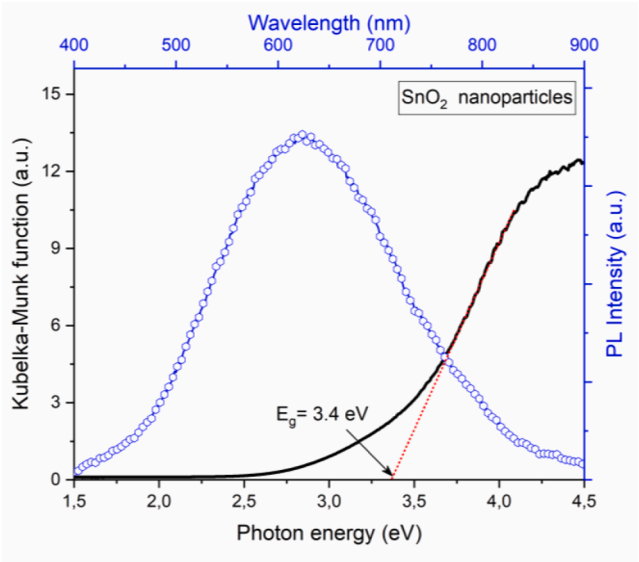

Fig. 3. Black curve (axis on the right): Kubelka-Munk equation used to estimate the optical gap (E_g) of the nanocrystalline SnO_2 sample. Blue curve (axis on the left) PL spectrum of SnO_2 nanoparticles.

heat treatment are displayed in Fig. 1**(a)**. It can be seen that the as-obtained sample presents a typical amorphous XRD pattern and, after the annealing process XRD peaks were observed. These XRD reflections confirm that the crystalline structure was obtained. Additionally, they match the tetragonal rutile phase of SnO_2, according to Joint Committee on Powder Diffraction Standards (file #36-1451). With regard to the morphological features, Fig. 1**(b)** shows an HRTEM micrograph of the crystalline SnO_2 sample. An analysis of this image reveals that the nanometric characteristic of the particles remains with an average size of 6 nm even after heat treatment. Moreover, the inset in Fig. 1**(b)** presents the interplanar distance of (110) crystallographic plane of the SnO_2 phase, which is approximately 0.33 nm. [43,44]

Theoretical results for bulk and surface models of SnO_2 are summarized in Fig. 2, indicating the building blocks that describe the crystalline structure. It can be seen that the calculated lattice parameters for SnO_2 were $a = b = 4.664$ Å and $c = 3.155$ Å, which are in accordance with previous theoretical and experimental results. [39–41] The building block of SnO_2 is the [SnO_6] cluster, which is composed of two short (2.018 Å) and four long (2.031 Å) Sn-O bonds. For the (100) and (110) surface models, the existence of a single dangling bond forming under-coordinated [SnO_5] centers can be noted. The significant difference between the surface models can be attributed to the [SnO_5] orientation and the presence of superficial [SnO_6] clusters along the (110) surface, inducing increased stability for the latter.

The optical absorbance measurement of the SnO_2 nanoparticles is displayed in Fig. 3, black curve. The optical band gap (E_g) values of both samples were determined using the Kubelka-Munk equation,[45] which provided a value of approximately 3.4 eV. This value is in accordance with that reported literature for the SnO_2 compound.[46,47]. Furthermore, an analysis of the SnO_2 spectrum (black curve, Fig. 3) reveals the existence of a tail extending close to around 2.8 eV, indicating the presence of intrinsic defects, mainly oxygen vacancies, capable of creating new electronic levels within the band gap. [48,49] In the same figure, (blue curve, Fig. 3), it is possible to observe that the photoluminescence (PL) spectrum of the SnO_2 nanoparticles consists of a broad emission band whose maximum is located at around 625 nm. According to the literature, the presence of such intermediate levels leads to a system in which the relaxation process happens by several

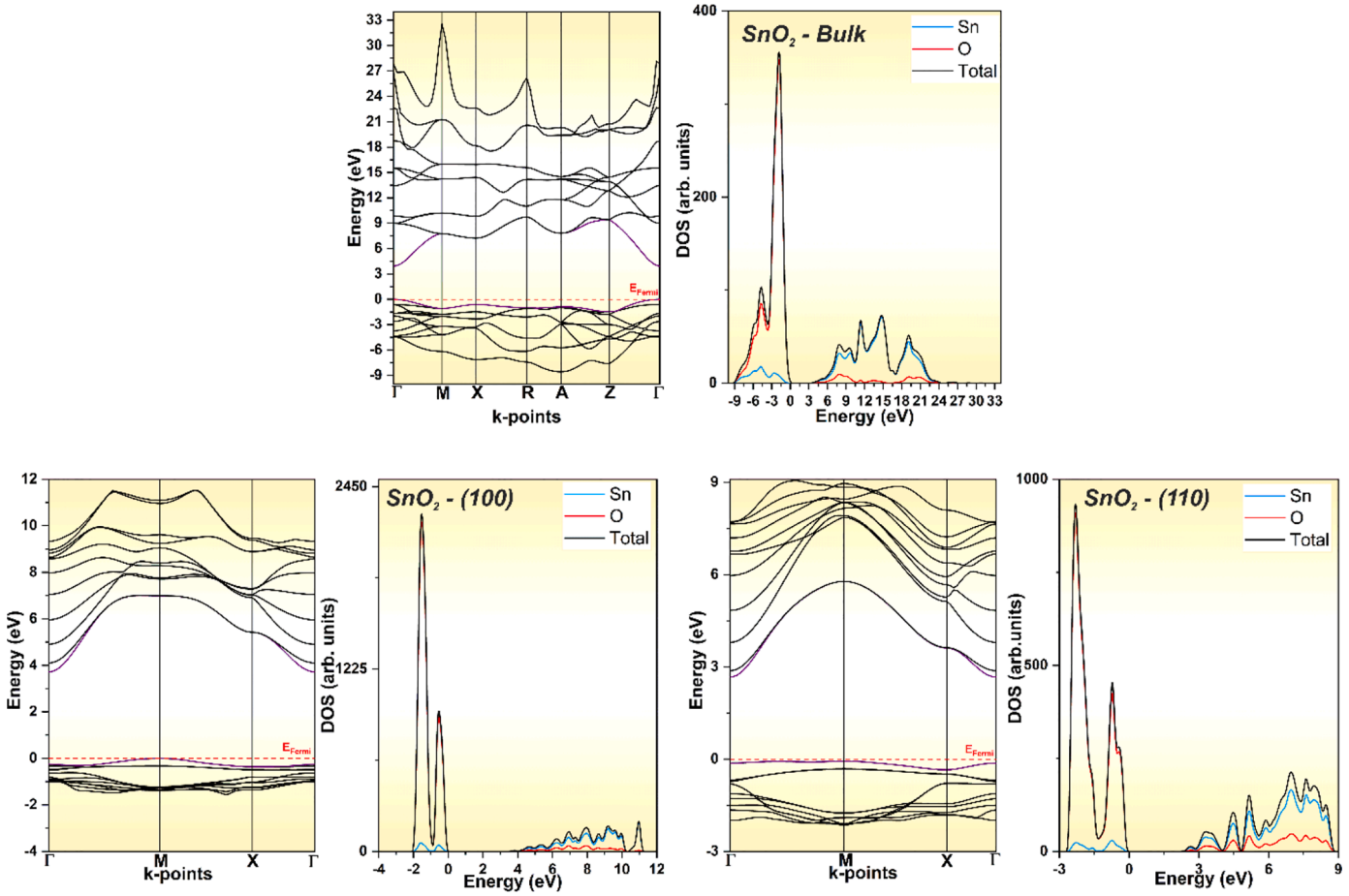

Fig. 4. Band Structure and atom-resolved Density of States profiles calculated for SnO_2bulk and surface models.

paths, thus originating a broad emission band. [50,51]. Bonu et al. reported that the PL emission around 625 nm can be attributed to defects created by oxygen vacancies in the SnO_2 lattice. [44] Similarly, Kar et al. conducted a detailed experimental investigation on the PL properties of SnO_2 nanorods and nanoparticles. [52] According to their findings, the PL emission can be linked to a transition of an electron from a level close to the conduction band edge to a deeply trapped hole in the bulk. [52] Therefore, the presence of such oxygen vacancies (here suggested by XPS analysis, Fig.S1) contribute to the formation of new levels in the band gap region of the SnO_2, enabling that longer excitation wavelengths generate charge carriers in the sensing layer. [15,53].

Regarding the electronic properties of SnO_2, DFT calculations were carried out for both bulk and surface models to describe the bandgap region. For the bulk model (central panel of Fig. 4), it can be observed that the valence band is mainly composed of O (2p) states, while the conduction band is formed by Sn (5sp) states. The electronic band gap was calculated as a direct transition equal to 3.92 eV, which is close to the obtained experimental results. The electronic states distribution remains equal for the (100) and (110) surface models, whilst the electronic band gap reduces to 3.72 and 2.67 eV, respectively. The band gap narrowing can be associated with the chemical environment of the exposed surfaces, i.e., the undercoordinated Sn centers induce the creation of intermediary states that contribute to reducing the required energy for electronic excitation.

The ozone gas-sensing properties of the nanocrystalline SnO_2 sample was studied under continuous illumination using certain excitation wavelengths, i.e., UV, violet and blue. Note that the sample was also exposed to ozone gas in a dark mode to verify the effect of illumination . **Fig. 5(a)** shows the response of the SnO_2 nanoparticles exposed to 12 ppb of O_3 in the absence of any light stimulation (dark mode). As observed, the sensing activity is apparently null, however, a closer view reveals a very low response, beyond the non-desorption of the O_3 molecules. It means that this configuration (dark mode and room temperature) did not provide enough energy to get an efficient desorption of the O_3 molecules from the sensing surface.

To evaluate the effect of light stimulation on the ozone gas-sensing performance, the sample was then submitted to different ozone levels (**Fig. 5(b)-(d)**). These measurements were performed at room-temperature, keeping the sample under continuous illumination stimulation and, only varying the wavelength of light source.

For the three distinct wavelengths studied, the sample presented sensing activity when exposed to different O_3 levels, always achieving full recovery after each exposure cycle. From the analysis of Fig. 5, it is evident that the employment of a certain wavelength to assist in the sensing process affects considerably the adsorption and desorption processes. These findings suggest that the energy of the photons provided by the light source may be used to tune the ozone sensing performance of SnO_2 nanoparticles.

Fig. 6(a) displays the sensor response curve of the nanocrystalline SnO_2 sample exposed to different ozone levels when irradiated by different light sources (UV, violet and blue). These data were extracted from **Fig. 5**, and show an enhancement of the sensor response with increasing ozone level for all light sources here investigated. In fact, Fig. 6(a) confirms that the sensor response depends on the wavelength chosen to perform the light-assisted sensing measurements. The observed order of gas-sensing performance is UV > violet > blue. Note that for the lowest analyte concentration (12 ppb) the wavelength chosen did not affect the sample response, indicating low accuracy of the sample for very low ozone levels.

Regarding the wavelength of the light source employed in the

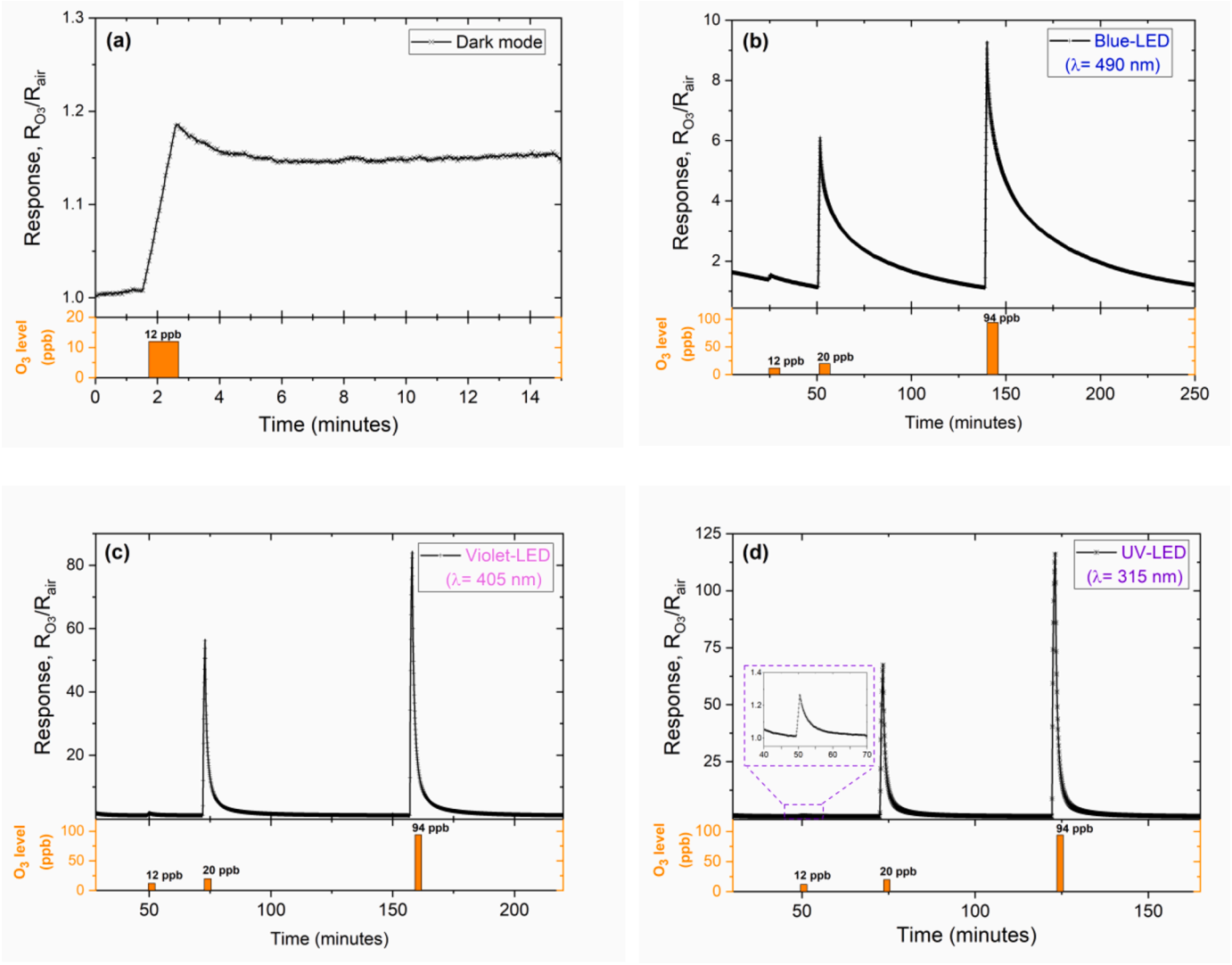

Fig. 5. Room-temperature gas sensing response of nanocrystalline SnO_2 sample exposed to different O_3 levels (12, 20, 94 ppb) and continuously assisted by a light source. (a) without any illumination "dark mode", (b) blue, (c) violet, and (e) UV-light.

sensing experiments, the UV source has been widely explored. [10,11, 15,53] Its choice is based on the band gap energy of the sensing material. However, as previously discussed the presence of different defects in the nanocrystalline SnO_2 makes wavelengths in the visible region useful for assisting ozone gas-sensing measurements. It can be seen in Fig. 6**(b)** that the ozone sensing response depends on the wavelength of the light source used to assist the SnO_2 sample. It is noteworthy that the sample detected the O_3 gas (presenting total recovery) when illuminated by the following wavelengths: UV, violet and blue, with no sensing activity when irradiated by green light. An analysis of the curve presented in Fig. 6**(b)** reveals a significant reduction in the sensor response at longer wavelengths, demonstrating the importance of photogenerated charge carriers in the detection of O_3 molecules.

Table 1 presents the performance of some MOXs synthesized by different methodologies, applied as a light-assisted ozone gas sensing material. It can be seen, the minimum ozone level detected by SnO_2 nanoparticles is close to those reported for other MOXs. It demonstrated that the chemical synthesis here used is a facile method to prepare efficient ozone gas sensors.

Let us now analyze the ozone gas-sensing properties of SnO_2 and their relationship with light activation. For this purpose, the first analysis involves the electron and hole localization and the exposed (100) and (110) surfaces modeled from the addition and removal of electrons from previously optimized surfaces, as depicted in Fig. 7. The excited electron is localized on the undercoordinated $[SnO_5]$ cluster for both surfaces, while the hole is localized on the neighboring oxygen atoms. The significant difference is related to the hole localization. For the (100) surface, the hole is localized on the superficial oxygen atoms, i. e., the $[SnO_5]$ is directly involved in the electron-hole excitation and localization.

On the other hand, for the (110) surface the hole is localized on the neighboring $[SnO_6]$ cluster, reducing the probability of electron-hole recombination, and consequently increasing the reactivity. This fact follows the structural and electronic features reported above, where the existence of both $[SnO_5]$ and $[SnO_6]$ surfaces induce higher surface stability and increased reactivity despite the increased band gap value in comparison to the (100) surface. Therefore, even though the narrow band gap of the (100) surface induces an increased rate of electron-hole excitation using the visible spectra region (2.64 eV = 464.36 nm), the localization of excited charge carriers reduces the stability and increase the recombination rate in comparison to (110). In this context, it is possible to argue that the SnO_2 (110) surfaces are better for UV-assisted gas adsorption since the charge carriers remain stable.

In order to evaluate the gas-sensing property of the SnO_2 surfaces, the adsorption energy of O_3 was calculated considering neutral and charged surface models. The major structural features evaluated to

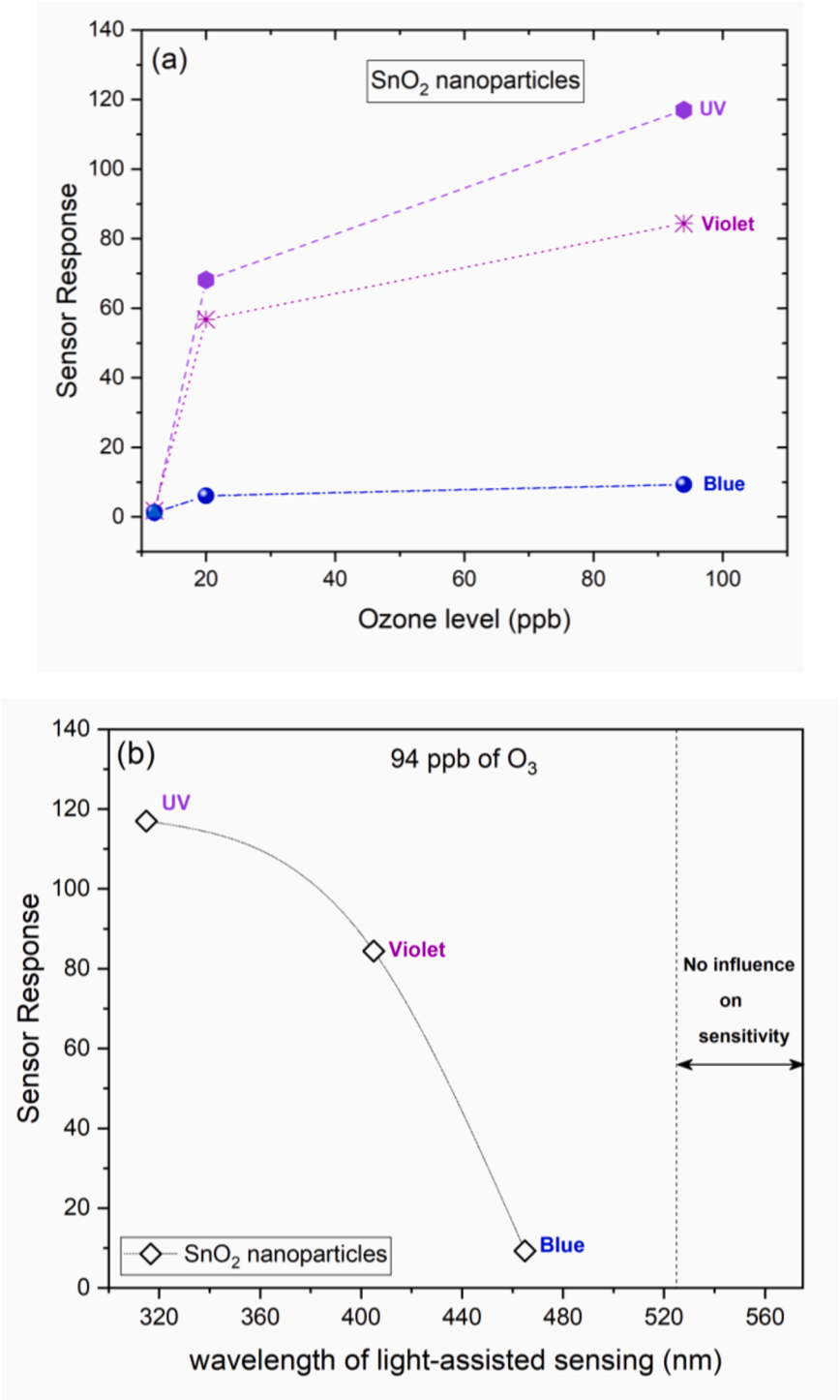

Fig. 6. Light-assisted ozone sensing response of nanocrystalline SnO_2 sample as a function of (a) ozone level and, (b) wavelength of light-assisted.

investigate the O_3 gas-sensing properties before and after electronic excitation are depicted in Fig. 8 and summarized in Table 2.

First, it can be observed that the O_3 adsorption occurs as two-point interactions for the (100) surface and one-point interaction for the (110) plane, resulting in superior adsorption energy for the former. Moreover, the distance between the O_3 molecule and the under-coordinated Sn center is smaller for the (100) surface, indicating that the neighboring [SnO_5] clusters contribute to induce a superior geometrical orientation that governs the adsorption mechanism. Furthermore, the ozone adsorption along both SnO_2 surfaces maintains the molecular geometry for O_3, indicating a reversible mechanism.

The most critical features analyzed from Table 2 are associated with the geometrical constraints resulting from the localization of excited electrons and holes. For the (100) surface, the localization of missing electrons (holes) points to a minor reduction of Sn-O_3 bond length, indicating that the adsorption energy does not increase with the hole localization. However, after the localization of adding charges (electrons), the Sn-O_3 distances reduce to a greater extent, demonstrating that excited electrons enhance the O_3 adsorption mechanism. These facts are related to the localization of electronic states reported in atom-resolved DOS (Fig. S3), where the obtained results for O_3 adsorption after electron localization suggests a different pattern associated with

Table 1
Room-temperature performance of the MOXs used as light-assisted ozone gas sensors.

Sensing material	Processing methodology	Light source / wavelength (nm)	O_3 level*(ppb)	Reference
SnO_2 thin film	Sputtering	UV-LED / 370	2000	[54]
ZnO nanorods	CVD	UV-lamp /366	500	[55]
ZnO microparticles	Precipitation followed by annealing	UV-LED / 400	10	[56]
In_2O_3 microparticles	Melt impregnation	Blue-LED / 460	50	[57]
In_2O_3 nanoparticles	MOCVD	UV-LED / 400	10	[58]
ZnO-SnO_2 nanocomposite	Hydrothermal	UV-LED / 325	20	[15]
SnO_2 nanoparticles	Precipitation followed by annealing	UV-LED / 315 Violet-LED / 405 Blue-LED / 465	12	This work

* Minimum O_3 level, experimentally, detected.

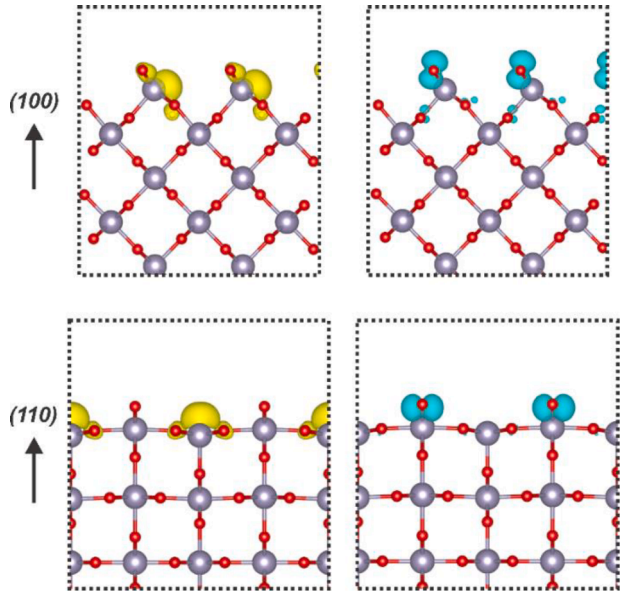

Figure 7. Spin density isosurface for (100) and (110) surface models of SnO_2 containing an adding (left) and missing (right) electron to model the electron-hole localization after excitation. The isovalue was set as 0.005 eV/Å^3.

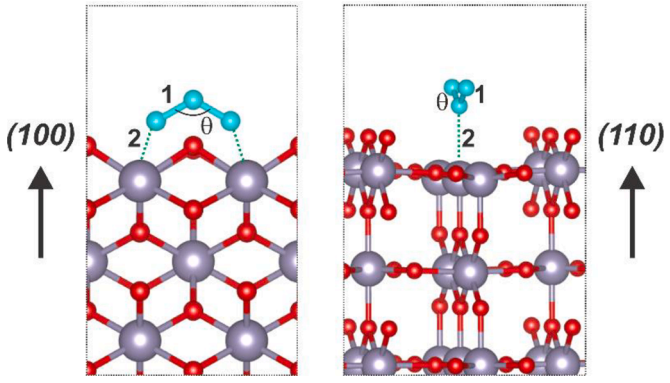

Figure 8. Optimized geometries for O_3 adsorption along with the (100) and (110) surface models of SnO_2 before the electron excitation.

the contribution of Sn centers, while the hole localization spreads out along all oxygen atoms of the exposed surface.

On the other hand, for the (110) surface the calculated Sn-O_3 bond distances after the localization of electrons and holes reduce almost by the same extent, indicating that both mechanisms increase the adsorption energy and O_3 gas-sensing properties. Such fact can be attributed to the presence of both [SnO_5] and [SnO_6] clusters along the exposed surface, which contribute to the localization of excited charge carriers in different crystalline sites, enhancing the O_3 adsorption mechanism for both electronic states, as presented in atom-resolved DOS (**Fig. S3**).

Table 2
Adsorption energy (E_{ads}) and structural parameters evaluated for O_3 adsorption along with the (100) and (110) surface models of SnO_2. The oxidized (+1) and reduced (-1) refer to the localization of missing and adding electrons, respectively.

Surface	Electronic state	E_{ads}(ev)	^{1}O-O (Å)	Θ	^{2}Sn-O (Å)
(100)	Neutral	-0.75	1.275	119.04	2.400
	Oxidized (+1)	-	1.269	119.68	2.389
	Reduced (-1)	-	1.343	121.66	2.185
(110)	Neutral	-0.33	1.261	119.79	2.546
	Oxidized (+1)	-	1.264	121.15	2.432
	Reduced (-1)	-	1.302	117.53	2.456

As previously discussed, the (110) surface exhibits an increased charge carrier stability since the electrons and holes are localized in distinct clusters, resulting in a reduced recombination rate. Therefore, the UV-assisted excitation generates photoexcited charges responsible for enhancing the O_3 sensing performance. In contrast, despite the band gap reduction (visible spectra) and increased adsorption energy for the (100) surface, the excited charge carriers exhibit a more effective recombination rate, which in turn reduces the O_3 sensing activity.

4. Conclusions

In summary, the pristine SnO_2 compound operating at room temperature under continuous light stimulation was investigated as an ozone gas sensor. XRD and HRTEM analyses confirmed the nanocrystalline characteristics of the sample after heat treatment. Electrical measurements revealed a dependence of ozone sensing performance on the wavelength of light stimulation. The maximum ozone response of the SnO_2 nanoparticles was reached under UV light, while no sensing activity was observed for light stimulation using a green light source. The DFT calculations used to support the experimental measurements showed the significant aspects associated with the stability of photogenerated carriers along the (100) and (110) surfaces of SnO_2 and confirmed that the presence of undercoordinated and regular Sn centers contributed to exciton dissociation on the (110) surface and increased adsorption energy after electronic excitation. We believe that the findings presented herein may be extended for further light-assisted sensing materials, such as ZnO, WO_3, and In_2O_3.

Declaration of Competing Interest

The authors declare that they have no known competing financial interests or personal relationships that could have appeared to influence the work reported in this paper.

Acknowledgments

The authors would like to thank the financial support provided by the Brazilian research financing institutions FAPESP (grant nos. 2018/18208-0, 2017/12437-5, 2021/01651-1 and 2013/07296-2), and CNPq (grant nos. 405140/2018-5 and 426511/2018-2). This research was partially performed at the Brazilian Nanotechnology National Laboratory (LNNano), Microfabrication laboratory (Project MNF-27743), Campinas, SP, Brazil. R. A. P. Ribeiro is grateful for the financial assistance from FAPEMIG (project no. APQ-00079-21) and UEMG for the Productivity Program. The authors thank the Federal University of Rio de Janeiro (COPPE-UFRJ) National Laboratory for Scientific Computing (LNCC) and High-Performance Computing Center (NACAD) for providing computational resources for the Lobo Carneiro supercomputer. The authors would also like to thank the National Center for High-Performance Computing (CENAPAD) at UNICAMP and UFMG for providing computing resources.

Supplementary materials

Supplementary material associated with this article can be found, in the online version, at doi:10.1016/j.snr.2022.100081.

References

[1] L.F. da Silva, A.C. Catto, S. Bernardini, T. Fiorido, J.V.N. de Palma, W. Avansi Jr, K. Aguir, M. Bendahan, BTEX gas sensor based on hematite microrhombuses, Sensors Actuators B Chem 326 (2021), 128817, https://doi.org/10.1016/j.snb.2020.128817.

[2] Y. Wu, J. Ward-Bond, D. Li, S. Zhang, J. Shi, Z. Jiang, g-C_3N_4@α-Fe_2O_3/C Photocatalysts: synergistically intensified charge generation and charge transfer for NADH regeneration, ACS Catal 8 (2018) 5664–5674, https://doi.org/10.1021/acscatal.8b00070.

[3] G.T.S.T. da Silva, K.T.G. Carvalho, O.F. Lopes, E.S. Gomes, A.R. Malagutti, V. R. Mastelaro, C. Ribeiro, H.A.J.L. Mourão, Synthesis of ZnO nanoparticles assisted by N sources and their application in the photodegradation of organic contaminants, ChemCatChem 9 (2017) 3795–3804, https://doi.org/10.1002/cctc.201700756.

[4] S. Hilaire, M.J. Suess, N. Kranzlin, K. Bienkowski, R. Solarska, J. Augustynski, M. Niederberger, Microwave-assisted nonaqueous synthesis of WO_3 nanoparticles for crystallographically oriented photoanodes for water splitting, J. Mater. Chem. A. 2 (2014) 20530–20537, https://doi.org/10.1039/C4TA04793A.

[5] M.L. Moreira, G.P. Mambrini, D.P. Volanti, E.R. Leite, M.O. Orlandi, P.S. Pizani, V. R. Mastelaro, C.O. Paiva-Santos, E. Longo, J.A. Varela, Hydrothermal Microwave: A new route to obtain photoluminescent crystalline $BaTiO_3$ nanoparticles, Chem. Mater. 20 (2008) 5381–5387, https://doi.org/10.1021/cm801638d.

[6] D.R. Miller, S.A. Akbar, P.A. Morris, Nanoscale metal oxide-based heterojunctions for gas sensing: A review, Sensors Actuators B Chem 204 (2014) 250–272, https://doi.org/10.1016/j.snb.2014.07.074.

[7] X. Zhou, S. Lee, Z. Xu, J. Yoon, Recent progress on the development of chemosensors for gases, Chem. Rev. 115 (2015) 7944–8000, https://doi.org/10.1021/cr500567r.

[8] G. Korotcenkov, A. Cerneavschi, V. Brinzari, A. Vasiliev, M. Ivanov, A. Cornet, J. Morante, A. Cabot, J. Arbiol, In_2O_3 films deposited by spray pyrolysis as a material for ozone gas sensors, Sensors Actuators B Chem 99 (2004) 297–303, https://doi.org/10.1016/J.SNB.2003.01.001.

[9] A. Favard, K. Aguir, T. Contaret, A. Dumas, M. Bendahan, Detection and measuring of BTEX traces at the ppb level using metal oxide gas sensor, Mater. Today Proc. 6 (2019) 323–327, https://doi.org/10.1016/j.matpr.2018.10.425.

[10] O. Casals, N. Markiewicz, C. Fabrega, I. Gràcia, C. Cané, H.S. Wasisto, A. Waag, J. D. Prades, A parts per billion (ppb) sensor for NO_2 with microwatt (μW) power requirements based on micro light plates, ACS Sensors 4 (2019) 822–826, https://doi.org/10.1021/acssensors.9b00150.

[11] O. Gonzalez, T. Welearegay, E. Llobet, X. Vilanova, Pulsed UV light activated gas sensing in tungsten oxide nanowires, Procedia Eng 168 (2016) 351–354, https://doi.org/10.1016/j.proeng.2016.11.118.

[12] E. Mudra, I. Shepa, O. Milkovic, Z. Dankova, A. Kovalcikova, A. Annušová, E. Majkova, J. Dusza, Effect of iron doping on the properties of SnO_2 nano/microfibers, Appl. Surf. Sci. 480 (2019) 876–881, https://doi.org/10.1016/j.apsusc.2019.03.041.

[13] N.D. Chinh, N.D. Quang, H. Lee, T. Thi Hien, N.M. Hieu, D. Kim, C. Kim, D. Kim, NO gas sensing kinetics at room temperature under UV light irradiation of In_2O_3 nanostructures, Sci. Rep. 6 (2016) 35066, https://doi.org/10.1038/srep35066.

[14] V. Postica, O. Lupan, A. Gapeeva, L. Hansen, R. Khaledialidusti, A.K. Mishra, J. Drewes, H. Kersten, F. Faupel, R. Adelung, S. Hansen, Improved long-term stability and reduced humidity effect in gas sensing: SiO_2 ultra-thin layered ZnO columnar films, Adv. Mater. Technol. 6 (2021), 2001137, https://doi.org/10.1002/admt.202001137.

[15] L.F. da Silva, J.-C. M'Peko, A.C. Catto, S. Bernardini, V.R. Mastelaro, K. Aguir, C. Ribeiro, E. Longo, UV-enhanced ozone gas sensing response of ZnO-SnO_2 heterojunctions at room temperature, Sensors Actuators B Chem 240 (2017) 573–579, https://doi.org/10.1016/j.snb.2016.08.158.

[16] S. Park, S. An, Y. Mun, C. Lee, UV-enhanced NO_2 gas sensing properties of SnO_2-Core/ZnO-shell nanowires at room temperature, ACS Appl. Mater. Interfaces. 5 (2013) 4285–4292, https://doi.org/10.1021/am400500a.

[17] J.M. Suh, T.H. Eom, S.H. Cho, T. Kim, H.W. Jang, Light-activated gas sensing: a perspective of integration with micro-LEDs and plasmonic nanoparticles, Mater. Adv. 2 (2021) 827–844, https://doi.org/10.1039/D0MA00685H.

[18] A.C. Catto, L.F. da Silva, M.B.I.B. Bernardi, M.S. Li, E. Longo, P.N. Lisboa-Filho, O. R. Nascimento, V.R. Mastelaro, An investigation into the influence of zinc precursor on the microstructural, photoluminescence, and gas-sensing properties of ZnO nanoparticles, J. Nanoparticle Res. 16 (2014) 2760, https://doi.org/10.1007/s11051-014-2760-0.

[19] O. Gonzalez, T.G. Welearegay, X. Vilanova, E. Llobet, Using the Transient Response of WO_3 Nanoneedles under Pulsed UV Light in the Detection of NH_3 and NO_2, Sensors (Basel). 18 (2018) 1346. https://doi.org/10.3390/s18051346.

[20] S. Liu, S. Gao, Z. Wang, T. Fei, T. Zhang, Oxygen vacancy modulation of commercial SnO_2 by an organometallic chemistry-assisted strategy for boosting acetone sensing performances, Sensors Actuators B Chem 290 (2019) 493–502, https://doi.org/10.1016/j.snb.2019.03.123.

[21] G. Korotcenkov, I. Blinov, M. Ivanov, J.R. Stetter, Ozone sensors on the base of SnO_2 films deposited by spray pyrolysis, Sensors Actuators B Chem 120 (2007) 679–686, https://doi.org/10.1016/J.SNB.2006.03.029.

[22] K. Suematsu, K. Watanabe, M. Yuasa, T. Kida, K. Shimanoe, Effect of ambient oxygen partial pressure on the hydrogen response of SnO_2 semiconductor gas sensors, J. Electrochem. Soc. 166 (2019) B618–B622, https://doi.org/10.1149/2.1391906jes.

[23] K.G. Godinho, A. Walsh, G.W. Watson, Energetic and electronic structure analysis of intrinsic defects in SnO_2, J. Phys. Chem. C. 113 (2009) 439–448, https://doi.org/10.1021/jp807753t.

[24] K. Anothainart, M. Burgmair, A. Karthigeyan, M. Zimmer, I. Eisele, Light enhanced NO_2 gas sensing with tin oxide at room temperature: conductance and work function measurements, Sensors Actuators B Chem 93 (2003) 580–584, https://doi.org/10.1016/S0925-4005(03)00220-X.

[25] Q. Geng, Z. He, X. Chen, W. Dai, X. Wang, Gas sensing property of ZnO under visible light irradiation at room temperature, Sensors Actuators B Chem 188 (2013) 293–297, https://doi.org/10.1016/j.snb.2013.07.001.

[26] C. Zhang, A. Boudiba, C. Bittencourt, R. Snyders, M.-G. Olivier, M. Debliquy, Visible light activated tungsten oxide sensors for NO_2 detection at room temperature, Procedia Eng 47 (2012) 116–119, https://doi.org/10.1016/j.proeng.2012.09.098.

[27] A. Chizhov, M. Rumyantseva, A. Gaskov, Light activation of nanocrystalline metal oxides for gas sensing: Principles, achievements, challenges, Nanomater. (2021) 11, https://doi.org/10.3390/nano11040892.

[28] D. Cho, J.M. Suh, S.-H. Nam, S.Y. Park, M. Park, T.H. Lee, K.S. Choi, J. Lee, C. Ahn, H.W. Jang, Y.-S. Shim, S. Jeon, Optically activated 3D thin-shell TiO_2 for super-sensitive chemoresistive responses: Toward visible light activation, Adv. Sci. 8 (2021), 2001883, https://doi.org/10.1002/advs.202001883.

[29] D. Liu, Z. Tang, Z. Zhang, Visible light assisted room-temperature NO_2 gas sensor based on hollow SnO_2@SnS_2 nanostructures, Sensors Actuators B Chem 324 (2020), 128754, https://doi.org/10.1016/j.snb.2020.128754.

[30] F.K.F. Oliveira, A.A.G. Santiago, A.C. Catto, L.F. da Silva, R.L. Tranquilin, E. Longo, F.V Motta, M.R.D. Bomio, Cerium molybdate nanocrystals: Microstructural, optical and gas-sensing properties, J. Alloys Compd. (2020), 157562, https://doi.org/10.1016/j.jallcom.2020.157562.

[31] W. Avansi, A.C. Catto, L.F. da Silva, T. Fiorido, S. Bernardini, V.R. Mastelaro, K. Aguir, R. Arenal, One-dimensional V_2O_5/TiO_2 heterostructures for chemiresistive ozone sensors, ACS Appl. Nano Mater. 2 (2019) 4756–4764, https://doi.org/10.1021/acsanm.9b00578.

[32] A.C. Catto, T. Fiorido, É.L.S. Souza, W. Avansi, J. Andres, K. Aguir, E. Longo, L. S. Cavalcante, L.F. da Silva, Improving the ozone gas-sensing properties of $CuWO_4$ nanoparticles, J. Alloys Compd. 748 (2018) 411–417, https://doi.org/10.1016/j.jallcom.2018.03.104.

[33] L.F. da Silva, A.C. Catto, W. Avansi, L.S. Cavalcante, J. Andres, K. Aguir, V. R. Mastelaro, E. Longo, A novel ozone gas sensor based on one-dimensional (1D) α-Ag_2WO_4 nanostructures, Nanoscale 6 (2014) 4058–4062, https://doi.org/10.1039/C3NR05837A.

[34] A.C. Catto, M.C. Oliveira, R.A.P. Ribeiro, W. Avansi, L.F. da Silva, E. Longo, Hematite rhombuses for chemiresitive ozone sensors: Experimental and theoretical approaches, Appl. Surf. Sci. 563 (2021), 150209, https://doi.org/10.1016/j.apsusc.2021.150209.

[35] A.D. Becke, Density-functional exchange-energy approximation with correct asymptotic behavior, Phys. Rev. A. 38 (1988) 3098–3100, https://doi.org/10.1103/PhysRevA.38.3098.

[36] C. Lee, W. Yang, R.G. Parr, Development of the colle-salvetti correlation-energy formula into a functional of the electron density, Phys. Rev. B. (1988), https://doi.org/10.1103/PhysRevB.37.785.

[37] S. Grimme, J. Antony, S. Ehrlich, H. Krieg, A consistent and accurate ab initio parametrization of density functional dispersion correction (DFT-D) for the 94 elements H-Pu, J. Chem. Phys. 132 (2010), 154104, https://doi.org/10.1063/1.3382344.

[38] R. Dovesi, A. Erba, R. Orlando, C.M. Zicovich-Wilson, B. Civalleri, L. Maschio, M. Rérat, S. Casassa, J. Baima, S. Salustro, B. Kirtman, Quantum-mechanical

condensed matter simulations with CRYSTAL, Wiley Interdiscip. Rev. Comput. Mol. Sci. (2018), https://doi.org/10.1002/wcms.1360.
[39] L. Gracia, A. Beltrán, J. Andrés, Characterization of the high-pressure structures and phase transformations in SnO_2. A Density Functional Theory Study, J. Phys. Chem. B. 111 (2007) 6479–6485, https://doi.org/10.1021/jp067443v.
[40] M. Calatayud, J. Andrés, A. Beltrán, A theoretical analysis of adsorption and dissociation of CH_3OH on the stoichiometric SnO_2(110) surface, Surf. Sci. 430 (1999) 213–222, https://doi.org/10.1016/S0039-6028(99)00507-5.
[41] F.R. Sensato, R. Custódio, M. Calatayud, A. Beltrán, J. Andrés, J.R. Sambrano, E. Longo, Periodic study on the structural and electronic properties of bulk, oxidized and reduced SnO_2(110) surfaces and the interaction with O_2, Surf. Sci. 511 (2002) 408–420, https://doi.org/10.1016/S0039-6028(02)01542-X.
[42] H.J. Monkhorst, J.D. Pack, Special points for Brillouin-zone integrations, Phys. Rev. B. 13 (1976) 5188–5192, https://doi.org/10.1103/PhysRevB.13.5188.
[43] D.A. Mirabella, P.M. Desimone, M.A. Ponce, C.M. Aldao, L.F. da Silva, A.C. Catto, E. Longo, Effects of donor density on power-law response in tin dioxide gas sensors, Sensors Actuators B Chem 329 (2021), 129253, https://doi.org/10.1016/j.snb.2020.129253.
[44] V. Bonu, A. Das, S. Amirthapandian, S. Dhara, A.K. Tyagi, Photoluminescence of oxygen vacancies and hydroxyl group surface functionalized SnO_2 nanoparticles, Phys. Chem. Chem. Phys. 17 (2015) 9794–9801, https://doi.org/10.1039/C5CP00060B.
[45] P. Kubelka, F. Munk, Ein Beitrag zur Optik der Farbanstriche, Zeitschrift Technol. Phys. 12 (1931) 593–600.
[46] W. Wu, L. Liao, S. Zhang, J. Zhou, X. Xiao, F. Ren, L. Sun, Z. Dai, C. Jiang, Non-centrosymmetric Au–SnO_2 hybrid nanostructures with strong localization of plasmonic for enhanced photocatalysis application, Nanoscale 5 (2013) 5628–5636, https://doi.org/10.1039/C3NR00985H.
[47] Y. Liu, S. Wei, G. Wang, J. Tong, J. Li, D. Pan, Quantum-Sized SnO_2 Nanoparticles with Upshifted Conduction Band: A Promising Electron Transportation Material for Quantum Dot Light-Emitting Diodes, Langmuir 36 (2020) 6605–6609, https://doi.org/10.1021/acs.langmuir.0c00107.
[48] S.H. Sun, G.W. Meng, G.X. Zhang, T. Gao, B.Y. Geng, L.D. Zhang, J. Zuo, Raman scattering study of rutile SnO_2 nanobelts synthesized by thermal evaporation of Sn powders, Chem. Phys. Lett. 376 (2003) 103–107, https://doi.org/10.1016/S0009-2614(03)00965-5.
[49] D. Guo, C. Hu, First-principles study on the electronic structure and optical properties for SnO_2 with oxygen vacancy, Appl. Surf. Sci. 258 (2012) 6987–6992, https://doi.org/10.1016/j.apsusc.2012.03.149.
[50] L.F. da Silva, L.J.Q. Maia, M.I.B. Bernardi, J.A. Andrés, V.R. Mastelaro, An improved method for preparation of $SrTiO_3$ nanoparticles, Mater. Chem. Phys. 125 (2011) 168–173, https://doi.org/10.1016/j.matchemphys.2010.09.001.
[51] V.M. Longo, A.T. de Figueiredo, S. de Lázaro, M.F. Gurgel, M.G.S. Costa, C. O. Paiva-Santos, J.A. Varela, E. Longo, V.R. Mastelaro, F.S.DE Vicente, A. C. Hernandes, R.W.A. Franco, Structural conditions that leads to photoluminescence emission in $SrTiO_3$: An experimental and theoretical approach, J. Appl. Phys. 104 (2008) 23515, https://doi.org/10.1063/1.2956741.
[52] A. Kar, S. Kundu, A. Patra, Surface Defect-Related Luminescence Properties of SnO_2 Nanorods and Nanoparticles, J. Phys. Chem. C. 115 (2011) 118–124, https://doi.org/10.1021/jp110313b.
[53] N. Joshi, L.F. da Silva, F.M. Shimizu, V.R. Mastelaro, J.-C. M'Peko, L. Lin, O. N. Oliveira, UV-assisted chemiresistors made with gold-modified ZnO nanorods to detect ozone gas at room temperature, Microchim. Acta. 186 (2019) 418, https://doi.org/10.1007/s00604-019-3532-4.
[54] C.-C. Jeng, P.J.H. Chong, C.-C. Chiu, G.-J. Jiang, H.-J. Lin, R.-J. Wu, C.-H.A. Wu, Dynamic equilibrium method for the SnO_2-based ozone sensors using UV-LED continuous irradiation, Sensors Actuators B Chem 195 (2014) 702–706, https://doi.org/10.1016/j.snb.2014.01.034.
[55] F.S.-S. Chien, C.-R. Wang, Y.-L. Chan, H.-L. Lin, M.-H. Chen, R.-J. Wu, Fast-response ozone sensor with ZnO nanorods grown by chemical vapor deposition, Sensors Actuators B Chem 144 (2010) 120–125, https://doi.org/10.1016/j.snb.2009.10.043.
[56] M.C. Carotta, A. Cervi, A. Fioravanti, S. Gherardi, A. Giberti, B. Vendemiati, D. Vincenzi, M. Sacerdoti, A novel ozone detection at room temperature through UV-LED-assisted ZnO thick film sensors, Thin Solid Films 520 (2011) 939–946, https://doi.org/10.1016/j.tsf.2011.04.173.
[57] D. Klaus, D. Klawinski, S. Amrehn, M. Tiemann, T. Wagner, Light-activated resistive ozone sensing at room temperature utilizing nanoporous In_2O_3 particles: Influence of particle size, Sensors Actuators B Chem 217 (2015) 181–185, https://doi.org/10.1016/j.snb.2014.09.021.
[58] C.Y. Wang, R.W. Becker, T. Passow, W. Pletschen, K. Köhler, V. Cimalla, O. Ambacher, Photon stimulated sensor based on indium oxide nanoparticles I: Wide-concentration-range ozone monitoring in air, Sensors Actuators B Chem 152 (2011) 235–240, https://doi.org/10.1016/j.snb.2010.12.014.